Biomedical Optics EXPRESS

Spatial light modulator based active wide-field illumination for *ex vivo* and *in vivo* quantitative NIR FRET imaging

Lingling Zhao,[1] Ken Abe,[2] Shilpi Rajoria,[2] Qi Pian,[1] Margarida Barroso,[2] and Xavier Intes[1,*]

[1]*Department of Biomedical Engineering, Rensselaer Polytechnic Institute, 110 8th Street, Troy, NY 12180, USA*
[2]*Center for Cardiovascular Sciences, Albany Medical College, 43 New Scotland Avenue, Albany, NY 12208, USA*
[*]*intesx@rpi.edu*

Abstract: Fluorescence lifetime imaging is playing an increasing role in drug development by providing a sensitive method to monitor drug delivery and receptor-ligand interactions. However, the wide dynamic range of fluorescence intensity emitted by *ex vivo* and *in vivo* samples presents challenges in retrieving information over the whole subject accurately and quantitatively. To overcome this challenge, we developed an active wide-field illumination (AWFI) strategy based on a spatial light modulator that acquires optimal fluorescence signals by enhancing the dynamic range, signal to noise ratio, and estimation of lifetime-based parameters. We demonstrate the ability of AWFI to estimate Förster resonance energy transfer (FRET) donor fraction from dissected organs with high accuracy (standard deviation <6%) over the whole field of view, in contrast with the homogenous wide-field illumination. We further report its successful application to quantitative FRET imaging in a live mouse. AWFI allows improved detection of weak signals and enhanced quantitative accuracy in *ex vivo* and *in vivo* molecular fluorescence quantitative imaging. The technique allows for robust quantitative estimation of the bio-distribution of molecular probes and lifetime-based parameters over an extended imaging field exhibiting a large range of fluorescence intensities and at a high acquisition speed (less than 1 min).

OCIS codes: (260.2510) Fluorescence; (170.6920) Time-resolved imaging; (170.3650) Lifetime-based sensing; (170.2945) Illumination design; (230.6120) Spatial light modulators; (260.2160) Energy transfer.

References and links

1. A. J. Fischman, N. M. Alpert, and R. H. Rubin, "Pharmacokinetic imaging: a noninvasive method for determining drug distribution and action," Clin. Pharmacokinet. **41**(8), 581–602 (2002).
2. D. J. Bornhop, C. H. Contag, K. Licha, and C. J. Murphy, "Advance in contrast agents, reporters, and detection," J. Biomed. Opt. **6**(2), 106–110 (2001).
3. T. F. Massoud, A. Singh, and S. S. Gambhir, "Noninvasive molecular neuroimaging using reporter genes: part II, experimental, current, and future applications," AJNR Am. J. Neuroradiol. **29**(3), 409–418 (2008).
4. H. Kobayashi, Y. Hama, Y. Koyama, T. Barrett, C. A. Regino, Y. Urano, and P. L. Choyke, "Simultaneous multicolor imaging of five different lymphatic basins using quantum dots," Nano Lett. **7**(6), 1711–1716 (2007).
5. N. Kosaka, M. Ogawa, N. Sato, P. L. Choyke, and H. Kobayashi, "In vivo real-time, multicolor, quantum dot lymphatic imaging," J. Invest. Dermatol. **129**(12), 2818–2822 (2009).
6. M. Y. Berezin and S. Achilefu, "Fluorescence lifetime measurements and biological imaging," Chem. Rev. **110**(5), 2641–2684 (2010).
7. H. Wallrabe and A. Periasamy, "Imaging protein molecules using FRET and FLIM microscopy," Curr. Opin. Biotechnol. **16**(1), 19–27 (2005).
8. S. Kumar, D. Alibhai, A. Margineanu, R. Laine, G. Kennedy, J. McGinty, S. Warren, D. Kelly, Y. Alexandrov, I. Munro, C. Talbot, D. W. Stuckey, C. Kimberly, B. Viellerobe, F. Lacombe, E. W. Lam, H. Taylor, M. J. Dallman, G. Stamp, E. J. Murray, F. Stuhmeier, A. Sardini, M. Katan, D. S. Elson, M. A. Neil, C. Dunsby, and

#197596 - $15.00 USD Received 14 Nov 2013; revised 20 Jan 2014; accepted 31 Jan 2014; published 27 Feb 2014

P. M. French, "FLIM FRET technology for drug discovery: automated multiwell-plate high-content analysis, multiplexed readouts and application in situ," ChemPhysChem **12**(3), 609–626 (2011).
9. V. Venugopal, J. Chen, M. Barroso, and X. Intes, "Quantitative tomographic imaging of intermolecular FRET in small animals," Biomed. Opt. Express **3**(12), 3161–3175 (2012).
10. S. A. Hilderbrand and R. Weissleder, "Near-infrared fluorescence: application to in vivo molecular imaging," Curr. Opin. Chem. Biol. **14**(1), 71–79 (2010).
11. L. Zhao, K. Abe, M. Barroso, and X. Intes, "Active wide-field illumination for high-throughput fluorescence lifetime imaging," Opt. Lett. **38**(19), 3976–3979 (2013).
12. V. Venugopal, J. Chen, and X. Intes, "Development of an optical imaging platform for functional imaging of small animals using wide-field excitation," Biomed. Opt. Express **1**(1), 143–156 (2010).
13. D. W. Bartlett, H. Su, I. J. Hildebrandt, W. A. Weber, and M. E. Davis, "Impact of tumor-specific targeting on the biodistribution and efficacy of siRNA nanoparticles measured by multimodality in vivo imaging," Proc. Natl. Acad. Sci. U.S.A. **104**(39), 15549–15554 (2007).
14. V. Venugopal and X. Intes, "Adaptive wide-field optical tomography," J. Biomed. Opt. **18**(3), 036006 (2013).
15. V. Venugopal, "A small animal time-resolved optical tomography platform using wide-field excitation," Doctoral Dissertation Rensselaer Polytechnic Institute, 47–49 (2011).
16. K. Abe, L. Zhao, A. Periasamy, X. Intes, and M. Barroso, "Non-Invasive In Vivo Imaging of Near Infrared-labeled Transferrin in Breast Cancer Cells and Tumors Using Fluorescence Lifetime FRET," PLoS ONE **8**(11), e80269 (2013).
17. M. Kollner and J. Wolfrum, "How Many Photons Are Necessary for Fluorescence-Lifetime Measurements," Chem. Phys. Lett. **200**(1-2), 199–204 (1992).
18. H. Wallrabe, M. Elangovan, A. Burchard, A. Periasamy, and M. Barroso, "Confocal FRET microscopy to measure clustering of ligand-receptor complexes in endocytic membranes," Biophys. J. **85**(1), 559–571 (2003).
19. H. Wallrabe, M. Stanley, A. Periasamy, and M. Barroso, "One- and two-photon fluorescence resonance energy transfer microscopy to establish a clustered distribution of receptor-ligand complexes in endocytic membranes," J. Biomed. Opt. **8**(3), 339–346 (2003).
20. Transferrin-Vivo 750 Fluorescent Imaging Agent. Available at http://www.perkinelmer.com/Catalog/Product/ID/10091)," (2013).
21. C. Alric, I. Miladi, D. Kryza, J. Taleb, F. Lux, R. Bazzi, C. Billotey, M. Janier, P. Perriat, S. Roux, and O. Tillement, "The biodistribution of gold nanoparticles designed for renal clearance," Nanoscale **5**(13), 5930–5939 (2013).
22. C. R. Berry, P. Fisher, P. D. Koblik, W. G. Guilford, and W. H. Hornof, "Scintigraphic biodistribution and plasma kinetics of indium 111-labeled transferrin in dogs," Am. J. Vet. Res. **58**(11), 1188–1192 (1997).
23. A. L. Vavere and M. J. Welch, "Preparation, biodistribution, and small animal PET of 45Ti-transferrin," J. Nucl. Med. **46**(4), 683–690 (2005).
24. J. Meek and E. D. Adamson, "Transferrin in foetal and adult mouse tissues: synthesis, storage and secretion," J. Embryol. Exp. Morphol. **86**, 205–218 (1985).
25. M. K. Kuimova, G. Yahioglu, J. A. Levitt, and K. Suhling, "Molecular rotor measures viscosity of live cells via fluorescence lifetime imaging," J. Am. Chem. Soc. **130**(21), 6672–6673 (2008).
26. M. Hassan, J. Riley, V. Chernomordik, P. Smith, R. Pursley, S. B. Lee, J. Capala, and A. H. Gandjbakhche, "Fluorescence lifetime imaging system for in vivo studies," Mol. Imaging **6**(4), 229–236 (2007).
27. M. Pimpalkhare, J. Chen, V. Venugopal, and X. Intes, "Ex vivo fluorescence molecular tomography of the spine," Int. J. Biomed. Imaging **2012**, 942326 (2012).

1. Introduction

Imaging technologies play a crucial role in drug development by providing information on the drug effect as well as its distribution in tissues [1]. These measurements are essential during drug development in preclinical studies as new drugs can be precisely compared with standard therapies, or a series of analogues can be screened for further development on the basis of their performances in animal models. Currently, several imaging approaches have been used to collect precise physiological and pharmacological measurements in small preclinical animal models such as ultrasound, X-ray computed tomography (CT), positron emission tomography (PET), single photon emission computed tomography (SPECT), magnetic resonance imaging (MRI) and optical imaging. In preclinical settings, optical imaging approaches offer several unique and distinct advantages. First, optical markers emit low-energy near-infrared (NIR) photons that are less harmful than more energetic γ-rays emitted from radioactive markers (used in SPECT and PET, for instance) [2]. Second, optical methods typically offer high sensitivity (bioluminescence imaging 10^{-15} to 10^{-17} mol/L, PET ~10^{-11} to 10^{-12} mol/L and MRI ~10^{-3} to 10^{-5} mol/L) [3] and are relatively inexpensive. Last, optical methods offer the possibility to image numerous molecular targets with multiple

#197596 - $15.00 USD Received 14 Nov 2013; revised 20 Jan 2014; accepted 31 Jan 2014; published 27 Feb 2014

distinct agents similarly to immunofluorescence microscopy and fluorescence cytometry. Although nuclear imaging and MRI techniques can potentially perform simultaneous imaging of 2 (or at most 3) molecular targets under limited conditions, the optical method is still the only imaging modality that is able to simultaneously distinguish five or more separate fluorescent probes *in vivo* [4, 5].

Fluorescence imaging can be performed with two main methodological approaches: fluorescence intensity and fluorescence lifetime. In contrast to fluorescence intensity imaging, fluorescence lifetime imaging (FLIM) is less dependent on excitation intensity or fluorophore concentrations. Moreover, fluorescence lifetime is sensitive to biochemical and physical factors in the immediate environment of the probe, such as temperature, pH, calcium-ion concentration, oxygen, refractive index, polarity and viscosity [6]. Another important application of this technique is the ability to sense protein-protein interactions using Förster resonance energy transfer (FRET) [7]. FLIM can overcome the limitations caused by fluorescence intensity based FRET, such as spectral bleed-through and crosstalk. The combination of FLIM and FRET is a promising modality for monitoring the dynamics of therapeutic drug release in the treatment of diseases with high spatial and temporal resolution from *in vitro* [8] to *in vivo* [9].

Quantitative fluorescence imaging has been extensively used for *ex vivo* and *in vivo* studies. In preclinical application, *ex vivo* studies have been widely used for pharmacokinetics studies and biological impact of fluorescent drug-probes conjugates from sample tissues. In *in vivo* application, fluorescence imaging has been applied to investigate the metabolism and biological activity resulting from disease [10].

However, quantitative accuracy in non-invasive *ex vivo* and *in vivo* FLIM is challenged by the signal to noise ratio (SNR). In photon counting techniques, the SNR is typically shot-noise limited. At low photon counts, the shot noise is characterized by a Poisson distribution. Shot noise cannot be eliminated, though, as the number of counted signal photons increases, the shot noise contributes a smaller percentage of the signal resulting in an increased SNR. On the other hand, the large distribution in photons emitted by different organs is associated with their various abilities to bind and retain fluorescently labeled molecules. Furthermore, in non-invasive *in vivo* studies, these variations in fluorescence emission are compounded by the heterogeneous nature of the tissues and path length distribution associated with varying tissue thicknesses. If the fluorescence intensity variations fall outside of the acquisition system dynamic range, the strongest signals are saturated and/or the weakest signals are lost, it compromises quantitative bio-distribution studies. Moreover, the estimation of the lifetime becomes unreliable due to poor photon counts statistics as the fluorescence lifetime estimation is based on fitting the measured intensity decays to an appropriate exponential model. Therefore, there is the need to increase the SNR and dynamic range of acquired data over a large field of view to improve the accuracy and precision of quantitative FLIM measurements.

To overcome these challenges, we developed an active wide-field illumination (AWFI) based on a digital micromirror device (DMD) by adjusting not only the overall laser power but also the spatial distribution of the wide-field illumination and applied it to *in vitro* measurements in a multi-well plate setting [11]. AWFI is achieved by iteratively balancing the fluorescence signals at the maximum peak of the fluorescence decay curve over the illumination area until photon counts are optimized. In this work, we applied AWFI to *ex vivo* biodistributions and live mice imaging of transferrin (Tfn)-conjugated NIR fluorophores. We demonstrate that this method not only improves the SNR and sensitivity to weak signals for fluorescence lifetime analysis, but also reduces the noise and laser bleed-through with high-throughput capabilities and fast acquisition time.

#197596 - $15.00 USD Received 14 Nov 2013; revised 20 Jan 2014; accepted 31 Jan 2014; published 27 Feb 2014

2. Methods and materials

2.1 NIR FRET pair preparation

Alexa Fluor® 700 and Alexa Fluor® 750 (A20010 and A20011, Life Technologies Corporation, CA) were selected as NIR FRET donor and acceptor, respectively. The Förster distance of this FRET pair is 7.76nm. Alexa Fluor® 700 (AF700) and Alexa Fluor® 750 (AF750) dyes were conjugated onto human Tfn (T3309, Sigma-Aldrich Inc., MO). Firstly, Tfn was saturated with iron after incubation with a molar excess of ferrous ammonium sulfate and nitrilotriacetate sodium salt solution in water. Then, after saturation, Tfn was conjugated to AF700 or AF750 dyes by incubating 5 µl of 10 µg/µl of dye in dimethyl sulfoxide (DMSO) per 1 mg of Tfn at a concentration of 7 mg/ml solution. After 1 hour of gentle rotation in the dark, labeling was stopped by passage over a resin desalting column. Tfn-dye complexes were then concentrated using concentrators that excluded the flow-through of particles larger than 35kD. Samples showed an average degree of labeling of ~2 fluorophore molecules per Tfn molecule.

2.2 Animal preparation

Athymic nude female mice (6-12 week old) (BALBNU-F, Taconic, USA) were used for *ex vivo* and *in vivo* biodistribution studies. Mice imaging was performed under vapor anesthesia (EZ-SA800 System, E-Z Anesthesia, USA) using isofluorane and monitored using a physiological monitoring system (MouseOx Plus, STARR Life Sciences Corp., USA). Body temperature was maintained by an air warmer (Bair Hugger 50500, 3M Corporation, USA) during the whole imaging session. All animal protocols were conducted with approval by the Institutional Animal Care and Use Committee (IACUC) at both Albany Medical College and Rensselaer Polytechnic Institute.

2.2.1 Tail vein injection

Mice were injected with Tfn labeled AF 750 (AF750-Tfn) and/or Tfn labeled AF700 (AF700-Tfn) in the RPMI 1640 media at molar ratios of 0:1 and 2:1 (keeping the donor amounts constant at 40 µg /ml of Tfn) via the tail vein using a sterile 1 mL syringe and 27 and ½ gauge needle (BD, 309623). The total volume would be <240 µL for injection. For *ex vivo* biodistribution analysis, four mice were used. Mice were injected with AF750-Tfn and/or AF 700-Tfn at molar ratios of 0:1 and 2:1 via tail vein and sacrificed after 6-hour or 24-hour post tail vein injections. Based on the expression of transferrin receptor (TfnR) in different organs, five organs, i.e. liver, kidney, spleen, brain, and heart, were harvested from each mouse and washed thoroughly with phosphate buffered saline solution for *ex vivo* imaging. These five organs are also the common organs used for pharmacokinetics studies. For *in vivo* biodistribution analysis, one mouse after 6-hour post injection at A:D = 2:1 was used.

2.3 Wide-field fluorescence lifetime imaging system

The time-domain fluorescence lifetime imaging system based on a gated intensified CCD (ICCD) detection used in this work is described in detail in [12]. However, the structured illumination module was optimized via replacing the pico-projector by a digital micromirror device (DMD, DLP Discovery 4100 Kit and D2D module, Texas instruments Inc., Texas) and optical module (S2 + optics module, Texas instruments Inc., Texas). This DMD based structured illumination module creates a spatial distribution of light beams with a resolution of 1024 × 768 pixels and 256 grayscale levels.

The overview of the system (see Fig. 1) is described briefly below. A tunable Ti-Sapphire pulsed laser, Mai Tai HP ® (Spectra-Physics, Newport Corporation, CA) is used as the laser source. The laser operates in the NIR window (tunable from 690nm - 1020nm) with a repetition rate of 80MHz and pulse-width of 100fs. For all experiments described herein, the excitation wavelength was set at 695 nm. The overall laser power is adjustable using a

#197596 - $15.00 USD Received 14 Nov 2013; revised 20 Jan 2014; accepted 31 Jan 2014; published 27 Feb 2014

computer-controlled variable attenuator (Application Note 30, Newport Corporation, MA) based on the combination of a half-wave plate and a polarizer with a closed loop feedback control system. The laser beam exiting the power control assembly is coupled into a 400μm multimode fiber (NA = 0.22), and then it is collimated (HPUCO-25-690/950-M-35AC-UNL, OZ Optics, Ontario, Canada) and focused (62584, Edmund Optics, USA) into the integrator rod of the S2 + optical module. The transmitted fluorescence signal from the sample is spectrally filtered by an emission bandpass filter (FF01-720/13-25 for AF700 detection, Semrock, NY) and detected by the ICCD (PicoStar HR, LaVision GmbH, Germany). The ICCD allows the measurement up to 2^{12} (4096) photons per temporal bin with a spatial resolution of 1376 × 1040 pixels.

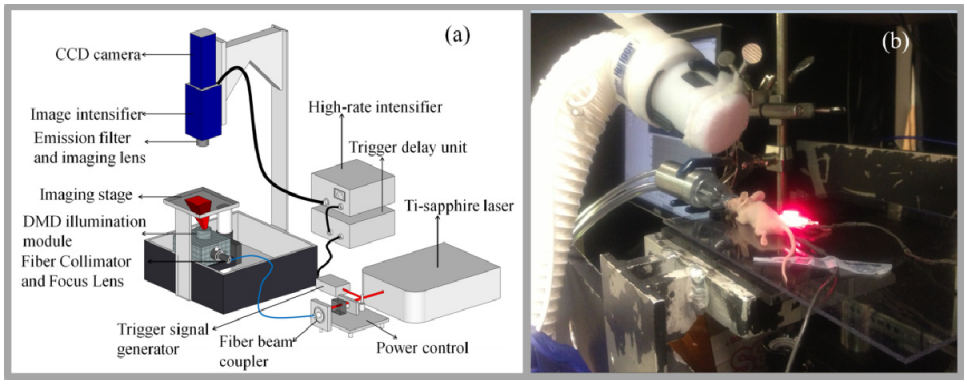

Fig. 1. Wide-field fluorescence lifetime imaging system for *ex vivo* and *in vivo* imaging. (a) The schematics of the time-domain fluorescence lifetime imaging system based on a gated ICCD detection. (b) The actual wide-field fluorescence lifetime imaging system for *in vivo* imaging.

The instrument response function (IRF) was measured by directly imaging a white diffusing paper placed on the stage. The gate-width on the ICCD camera was set to 300 ps. The IRF and the excitation signals were collected over a 2 ns time window at 40 ps resolution (50 gates) with the integration time of the camera set to 50 ms and the MCP voltage of 590 V for *ex vivo* and 610 V for *in vivo*. The measurements at the excitation wavelength for the complete set were acquired in 2.5s. The fluorescence signals were recorded over a 4.8 ns time window at 40 ps resolution (120 gates) with the integration time of 400 ms for *ex vivo* and 800ms for *in vivo*. The noise floor for this system with hardware binning (8 × 8) is less than 30 photon counts for *ex vivo* imaging and around 50-100 photon counts for *in vivo* imaging, due to different detector gains and integration times. The *ex vivo* and *in vivo* images were not binned post-acquisition before analysis and the pixel size is 0.5mm.

2.4 AWFI method

The detail of the AWFI method and its application to *in vitro* data can be found in [11]. Herein, we report its application to *ex vivo* and *in vivo* imaging. Briefly, the AWFI iterative procedure consists in optimizing the illumination pattern until the photon counts of the fluorescence signal reach the desired photon counts set by user at any given position over the full sample. The illumination pattern is created and modified under Microsoft PowerPoint (PPT) or via WindDraw VI of LabVIEW IMAQ (NI, USA). Similar to a common projector, the structured illumination module projects the pattern to the imaging stage for exciting the fluorescence signals. Because of the various fluorophore concentrations or the effects of the optical properties and thickness in the neighborhood of the fluorophores, different photon counts are detected by the ICCD. Due to the limited dynamic range of the ICCD, the system is then sensitive only to a small range of concentrations or certain fluorophores. Hence, quantitative lifetime estimation can be compromised for low concentrations or high the

#197596 - $15.00 USD Received 14 Nov 2013; revised 20 Jan 2014; accepted 31 Jan 2014; published 27 Feb 2014

effects of the optical properties and thickness in the neighborhood due to low photon counts acquired. Therefore, it is desirable to be able to optimize the illumination pattern in order to increase the overall dynamical range of the imaging platform and to acquire data with high photon counts for robust lifetime estimation. In this study, we set the desired photon counts at every pixel to be 3,600 for the maximum of the fluorescence temporal point-spread function (TPSF) based on the ICCD specifications.

Before AWFI, a binary mask was applied to the initial uniform illumination pattern to restrict the impinging power to the area of regions (ROIs). For *ex vivo* imaging, the binary mask was generated by the fluorescence images directly where all the organs were resolved. For *in vivo* imaging, both liver and bladder are expected to have high level of donor signals [13]. Thus, from the mouse anatomical locations and the strength of the fluorescence signals, the two organs were identified in the excitation image. The binary mask was generated by the excitation image directly, as shown in Media 3 left. To achieve the desired photon counts, the AWFI method utilizes the linear relationship between grayscale level in the illumination pattern and local power density. By iteratively optimizing both grayscale patterns and laser power, wide-field fluorescence emission can be collected with high photon counts. Practically, a new pattern is generated and applied for illumination with adjusted laser power at each iteration. For fast acquisition and optimization times, only fluorescence intensity image at the peak of the fluorescence TPSF is acquired and employed in the iterative process. The pattern is optimized iteratively until the stopping criteria reach preset conditions. The three stopping criteria used in the case where the integration time and detector gain are fixed, only laser power is unfixed are 1) Photon counts of the fluorescence signal reach the desired photon counts set by user over the fluorescence area; 2) The laser power doesn't change. 3) The laser power is up to the maximum. The AWFI can also adjust the integration time and detector gain to balance the gray levels supplied by the spatial light modulator. But we don't choose them because the adjustable range of integration time and detector gain is much smaller than the laser power (100 times and 10 times smaller, respectively) and non-linear relationship between the detector gain and the detected signals makes the optimization unwieldy.

2.5 Fluorescence lifetime fitting model

In this work, the lifetime distribution of the FRET-complex components was analyzed using a bi-exponential decay model wherein we estimated 4 unknown parameters – lifetimes and relative abundances of the FRET and nonFRET component of the donor molecules in the sample. For the temporal fluorescence decay function $\Gamma_{em}(t)$, the bi-exponential decay model is given by:

$$\Gamma_{em}(t) = IRF(t) \quad * \quad (N + \mathrm{FD} \cdot e^{-t/\tau FRET} + \mathrm{NFD} \cdot e^{-t/\tau nonFRET}) \qquad (1)$$

Here, FD and NFD are corresponding to FRET donor fraction and non-FRET donor fraction, τ_{FRET} and $\tau_{nonFRET}$ are the lifetime values for the two species. Also, N is an arbitrary additive factor introduced to account for the noise in the fluorescence TPSF. IRF was selected individually for each detector position. The measured fluorescence TPSF (from 98% to 1% of peak intensity leading typically to ~100 gates) is fitted to this model and the above four parameters are estimated using a nonlinear constrained minimization method based on sequential quadratic programming, fmincon (MATLAB, MathWorks, USA).

The fitting process for different A: D ratios was carried out in two steps. First, the fluorescence decay of donor only (A: D = 0:1) was fit with unbound lifetime estimates. The mean value of long lifetime (non-FRET donor) was then selected as a fixed parameter for the second step and τ_{FRET}, FD and NFD were estimated. The lifetime of the NFD and FD were estimated to be 1100 ± 100ps and 330 ± 50ps from *ex vivo* and *in vivo* data. It should be noted that R-square for each fitting curve is around 0.99.

#197596 - $15.00 USD Received 14 Nov 2013; revised 20 Jan 2014; accepted 31 Jan 2014; published 27 Feb 2014

3. Results and discussions

3.1 Calibration of active illumination module

The spatial light modulator DMD is an active optical element that affects the spatial, temporal and spectral performances of the time-domain imaging platform. Herein, we report the comprehensive characterization of the illumination module used in this study. First, illumination grayscale linearity and uniformity were measured (see Figs. 2(a)-2(b)). Second, the transmitted power efficiency of the illumination module was characterized at different wavelengths (see Fig. 2(c)). Third, the initial time t_0 and full width at half maximum (FWHM) of IRF were compared at different time gates and wavelengths (see Fig. 3).

As shown in Figs. 2(a)-2(b), the spatial fidelity of the DMD in projecting gray levels is characterized. The detected grayscale pattern is in good agreement with the input grayscale pattern. Especially, the low gray levels are within 3% of fidelity (c.f. Fig. 2(b)) whereas they were within 10% of accuracy when using the pico-projector [14]. Moreover, the overall spatial uniformity of the imaging platform, as measured as by imaging a homogenous input pattern, was characterized at ~85% [11].

Similarly, the transmitted power efficiency was calculated over the 695nm-820nm spectral range by estimating the slope of the curve between input laser power and output laser power (See Fig. 2(c)). For each wavelength, different levels of laser emission were set by the laser power controller. The input laser powers were measured before the light beam entered the DMD using a laser power meter (1916-C, Newport Corporation, MT). The output laser powers after DMD were measured by focusing the output wide-field pattern onto the surface of the same power meter using two biconvex lenses (LB1761-B, Thorlabs, NJ). Overall, the transmitted power efficiency ranges from 31% to 13% over the investigated spectral range. There is a notable reduction with increased wavelengths, due to the spectral sensitivity of the S2 + optics module. However, in the previous setup, the transmitted power efficiency of the pico-projector (PK101, Optoma, USA) was measured to be < 9% at 695nm. In comparison, the transmitted power efficiency of this DMD is improved by ~3.5 times [15].

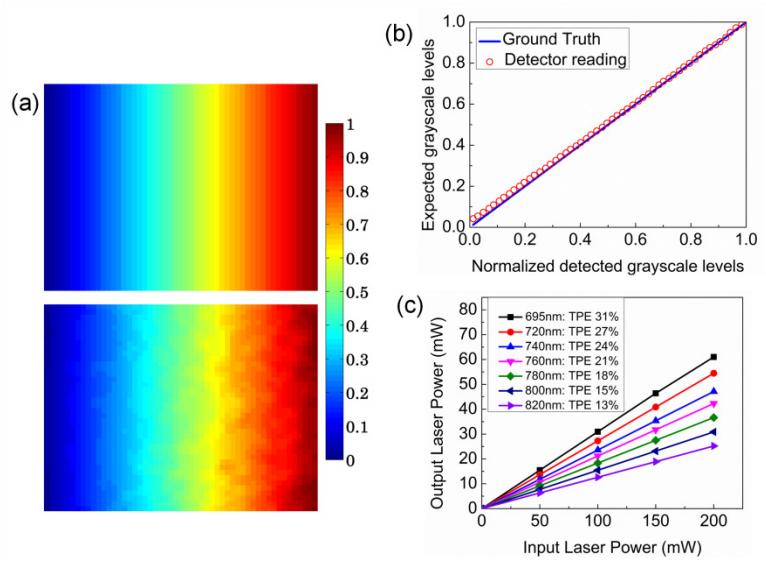

Fig. 2. Calibration of the spatial fidelity and transmitted power efficiency of the DMD. (a) Grayscale test pattern (top). Detected grayscale pattern normalized to the uniformed detected pattern (bottom). (b) Comparison of detected grayscale levels versus expected grayscale levels. (c) The Calibration of transmitted power efficiency of DMD. The transmitted power efficiency of DMD was calculated over the 695nm-820nm spectral range by estimating the slope of the curve between input laser power and output laser power. TPE: transmitted power efficiency.

#197596 - $15.00 USD Received 14 Nov 2013; revised 20 Jan 2014; accepted 31 Jan 2014; published 27 Feb 2014

To assess the effect of the DMD on the temporal characteristics of the system, an IRF was acquired for multiple gate-width settings (from 200ps to 1000ps at 100ps intervals). As expected, Figs. 3(a)-3(b) show that the gate-width has a significant impact on the FWHM of the IRF with minimal impact on the t_0 (947 ± 52ps). This is because the gate-width is the duration of time for which the ICCD camera shutter is open and then translated across the measurement time-window. Therefore, the impact of gate-width on the IRF can be defined as a temporal convolution of the laser pulse with a square function having width equal to the gate-width. As seen in Fig. 3(b), the IRF's FWHM is similar to the gate size, even in the case of the smallest gate-width (200ps), indicating that the DMD does not temporally broaden the laser pulse. Figures 3(c)-3(d) show that the IRF recorded for 4 wavelengths (695nm, 750nm, 800nm and 880nm) spanning the operational tuning range employed in the fluorescence imaging studies. The impact of the wavelength on the IRF is observed during the tuning operation. The t_0 is seen to shift by 360ps upon tuning from 695nm-880nm. The FWHM of the IRF of 300ps gate-width and 40ps gate-step is around 280ps and does not change significantly over the spectra investigated. Figures 3(e)-3(f) show that the t_0 and FWHM profiles along the center of the uniform pattern. The absolute value of Δt_0 is less than 35ps, which is smaller than the interval time (40ps) between two time gates for the fluorescence measurement used in this work. Thus, only one gate per fluorescence measurement can be used to optimize signal level.

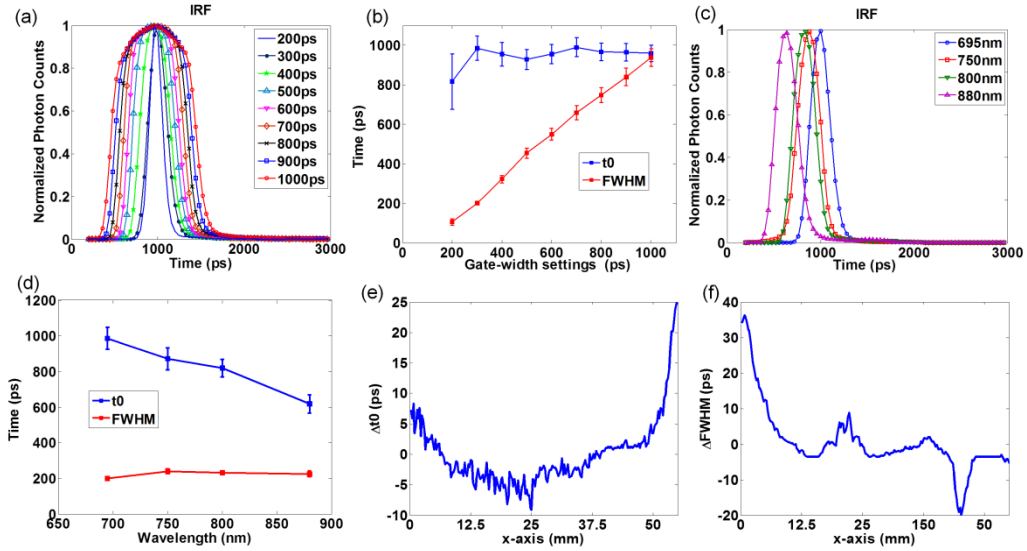

Fig. 3. Calibration of temporal characteristics of the DMD. (a) Effect of gate-width settings on IRF. (b) Impact of gate-width settings on IRF characteristics t_0 and FWHM. (c) IRF measured for various excitation wavelengths. (d) Impact of different excitation wavelengths on IRF characteristics t_0 and FWHM. (e) t_0 profile along the center of the uniform illumination pattern. (f) FWHM profile along the center of the uniform illumination pattern. IRF: instrument response function, t_0: the initial time, FWHM: full width at half maximum.

3.2 Active illumination for ex vivo biodistribution

In our previous work [16], we have demonstrated that AF700-Tfn behaves as a FRET donor that can effectively transfer energy to AF750-Tfn acceptor molecules upon internalization of Tfn-transferrin receptor (Tfn-TfnR) complexes into cancer cells using FLIM. We also have shown that FD% levels, which are directly correlated to FRET efficiency, are positively dependent on A:D ratios and independent of acceptor levels upon Tfn-TfnR binding and internalization into cancer cells. Therefore, this study focuses on evaluating FD % for *ex vivo and in vivo* bio-distributions.

#197596 - $15.00 USD Received 14 Nov 2013; revised 20 Jan 2014; accepted 31 Jan 2014; published 27 Feb 2014

Five organs (liver, kidney, spleen, brain, and heart) are distributed in one field of view (FOV, 35mm × 12mm) as shown in Fig. 4(a). The AWFI method was applied to the whole FOV to capture optimal transmitted fluorescence signal over the dissected organs at different A:D ratios (A:D = 0:1, A:D = 2:1) and various time points (6-hour and 24-hour post injections). The corresponding FD% before and after AWFI were calculated using Eq. (1).

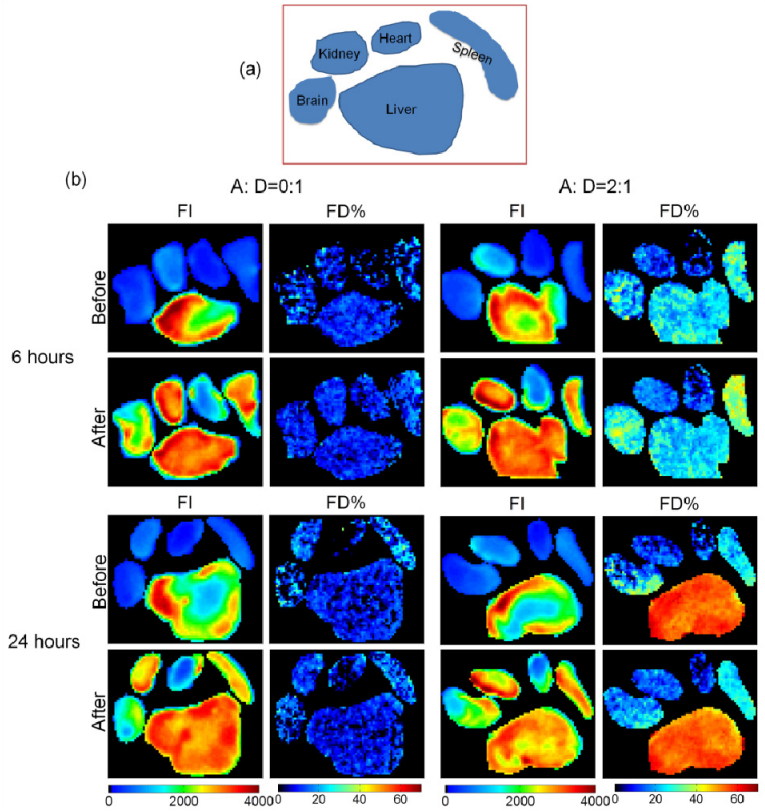

Fig. 4. (a) The imaging layout of five organs (Liver, kidney, spleen, brain and heart) distribution in one field of view (FOV, 35mm × 12mm). (b) Comparison between before and after AWFI using fluorescence intensity (FI) and FRET Donor fraction (FD %) from 6-hour and 24-hour injection at A:D = 0:1 and A:D = 2:1.

The fluorescence intensity (FI) and FD % before and after AWFI from different time points at A:D = 0:1 and A:D = 2:1 are visualized in Fig. 4(b). The AWFI performance is evaluated based on these images and discussed in section 3.2.1 in detail.

3.2.1 Evaluation of the AWFI performance for *ex vivo* biodistribution

To ensure that the evaluation of the performance before and after AWFI is consistent, a mask delineating the organs is generated at the start of the imaging session. As AWFI is a fast iterative process and that the samples are static, the mask before and after the iterative process are identical. AWFI and image analysis are applied within the boundary of the organs as defined by the mask.

The AWFI for *ex vivo* assessment of injected NIR FRET pair distribution in organs is applied to 4 different settings, which are A:D = 0:1 and A:D = 2:1 at 6-hour and 24-hour post tail vein injection. To simplify the description, we use the terms 6hr-A: D = 0:1, 6hr-A: D = 2:1, 24hr-A: D = 0:1 and 24hr-A: D = 2:1 for different mice from here onwards.

We evaluate the performance of AWFI method for *ex vivo* biodistribution by calculating the descriptive statistics from different dissected organs based on the images shown in Fig.

#197596 - $15.00 USD Received 14 Nov 2013; revised 20 Jan 2014; accepted 31 Jan 2014; published 27 Feb 2014

4(b). The descriptive statistics includes 1) mean photon counts, 2) mean FD %, and 3) coefficient of variation (CV) of FD %. The CV is defined as the ratio of the standard deviation to the mean. It shows the extent of variability on FD % over each organ with respect to the mean FD %.

Firstly, the mean photons from harvested organs are compared at different iteration numbers for the 4 cases shown in Fig. 5 (Media 1 and Media 2). As previously mentioned, for accurate fluorescence lifetime estimation by bi-exponential fitting, the photon counts need to be high, typically above 1,000 counts [17]. As shown in Fig. 5, before AWFI (iteration number = 0), of all the organs tested, only the liver from all four mice and kidney at 6hr-A: D = 2:1 have mean photon counts higher than 1,000 counts. Since the AWFI is applied to the whole FOV, the AWFI algorithm converges when the mean photon counts of all the organs reach a plateau in the iterative process. After AWFI algorithm converges, the mean photon counts of all the organs are above 1,000.

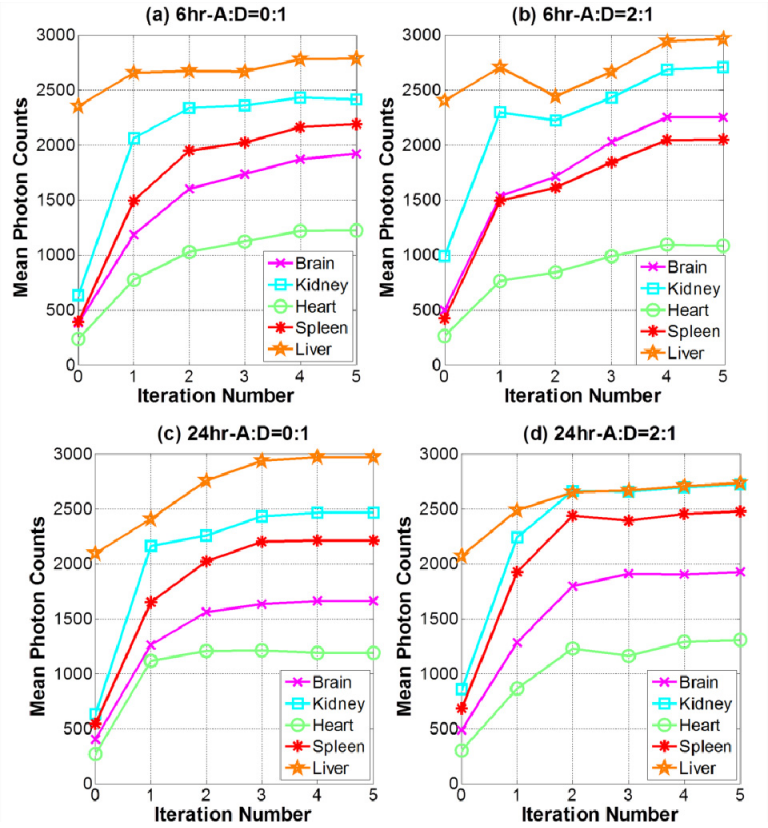

Fig. 5. The comparison of the mean photon counts of five organs (Liver, kidney, spleen, brain and heart) versus different iteration numbers. (a) A:D = 0:1 with post 6-hour injection (Media 1). (b) A:D = 2:1 with post 6-hour injection (Media 1). (c) A:D = 0:1 with post 24-hour injection (Media 2). (d) A:D = 2:1 with post 24-hour injection (Media 2). A: D = acceptor to donor ratio.

Note that AWFI algorithm stopped when the laser power did not change, without achieving the pre-defined photon count. In all cases investigated herein, the AWFI algorithm converges within 4 iterations for all the cases. The total acquisition time in each case was 49.6s (① Fluorescence acquisition for optimization, 1 time gate × 400 ms × 4 iterations = 1.6 s. ② Optimal fluorescence measurement, 120 time gates × 400 ms = 48 s).

#197596 - $15.00 USD Received 14 Nov 2013; revised 20 Jan 2014; accepted 31 Jan 2014; published 27 Feb 2014

Table 1. Comparison of FD% and CV% from 6-hour post injection

Organs	A:D = 0:1				A:D = 2:1			
	Before AWFI		After AWFI		Before AWFI		After AWFI	
	FD % ± STD	CV%	FD% ± STD	CV%	FD% ± STD	CV %	FD% ± STD	CV%
Liver	10 ± 4	40	9 ± 4	44	24 ± 5	21	23 ± 4	17
kidney	7 ± 6	86	9 ± 5	56	11 ± 6	55	16 ± 4	25
Spleen	8 ± 8	100	11 ± 5	45	28 ± 7	25	36 ± 5	14
Brain	8 ± 8	100	9 ± 5	56	20 ± 9	45	26 ± 5	19
Heart	3 ± 5	167	9 ± 5	56	5 ± 7	71	10 ± 5	50

Table 2. Comparison of FD% and CV% from 24-hour post injection

Organs	A:D = 0:1				A:D = 2:1			
	Before AWFI		After AWFI		Before AWFI		After AWFI	
	FD% ± STD	CV%	FD% ± STD	CV%	FD% ± STD	CV %	FD% ± STD	CV%
Liver	9 ± 5	56	8 ± 4	50	55 ± 4	7	54 ± 4	7
kidney	13 ± 7	54	12 ± 5	42	11 ± 5	45	14 ± 4	29
Spleen	15 ± 9	60	13 ± 6	46	24 ± 5	21	26 ± 3	12
Brain	9 ± 9	100	9 ± 6	67	20 ±	55	19 ± 5	26
Heart	6 ± 6	100	6 ± 5	83	8 ± 8	100	8 ± 5	63

Secondly, the mean FD%, and CVs of FD% from different excised organs are compared before and after AWFI at 4 cases shown in Table 1 and Table 2. All the values obtained from liver have no significant change before and after AWFI due to the high SNR. For other organs, the mean FDs% before and after AWFI are similar with the difference between 1% - 8%. The STDs of FD% after AWFI become more stable and smaller (<6%) than those before AWFI (>6%). The CVs of FD % after AWFI also become smaller than those before AWFI (see Table 1 and Table 2).

The overall of STDs and CVs of FD% at A:D = 0:1 are larger than those at A:D = 2:1. This is because FD% is positively dependent on A:D ratios and independent of acceptor levels in clustered interactions [9, 18, 19]. Specifically, the fluorescence intensity of donor is reduced when FRET occurs. The lower A:D ratio has higher intensity but lower FD%. The FRET signals are much reduced at A:D = 0:1 although the intensity is highest. The FRET signals are strongest at A:D = 2:1 although the intensity is lowest. Thus, the STDs and CVs at A:D = 0:1 were worse than those at A: D = 2:1. However, the accuracy in estimating the FD% is related to the photon counts (SNR). Thus, the STDs and CVs after AWFI become much smaller, which is significant for robust quantitative analysis.

3.2.2 The recovery of true intensity distribution

In pharmacokinetics studies, the fluorescence brightness is related to the tissue uptake and clearing of the molecular probe. Thus, to retrieve the true relative brightness of different organs, the recovered fluorescence image was generated by normalizing the optimized fluorescence image to the optimized illumination pattern image. Figures 6 and 7 give a comprehensive comparison of the fluorescence distributions and fluorescence intensities in

#197596 - $15.00 USD Received 14 Nov 2013; revised 20 Jan 2014; accepted 31 Jan 2014; published 27 Feb 2014

various organs obtained from the fluorescence image before AWFI and the recovered image, as well as the fluorescence image after AWFI. As seen in Fig. 6(a) and Fig. 7(a), the recovered fluorescence images have similar relative brightness to the ones before AWFI. Compared to the images before AWFI and recovered images, the ones after AWFI have better contrasts, more photon counts and show more homogenous fluorescence distributions in the liver, kidney and spleen.

As shown in Fig. 6(b) and Fig. 7(b), the normalized photon counts for the three-type fluorescence images were calculated in three steps. 1) Normalization: ① Before AWFI: the fluorescence image before AWFI is divided by excitation image of the non-optimized illumination pattern. ② The recovered image: the fluorescence images after AWFI divided by excitation image of the optimized illumination pattern. ③After AWFI: the fluorescence image after AWFI normalized by its maximum photon count. 2) The mean photon counts were calculated from the first step for each organ. 3) The mean photon count from the second step was normalized to maximum values for demonstrating the relative brightness. The photon counts in the recovered fluorescence image indicate that fluorescence probe is unevenly distributed in these organs with the following characteristics: 1) The strongest fluorescence signals are detected in the liver among all the organs at 6 hours and 24 hours. 2) The fluorescence signals of kidney and spleen are second to the liver. 3) The brain and heart have relatively less fluorescence signals. The brightness of fluorescence signals is related to the level of expression of TfnRs in these organs. The brain and heart have lower expression of TfnR compared to other mononuclear phagocytic cells-rich organs such as liver and spleen. Thus, the brain and heart show lower brightness of fluorescence signals. It should be noted that inflammatory cells such as monocytes express high levels of TfnRs allowing these organs to uptake more Tfn and subsequently sequester iron in the cells. These results are also consistent with the known behavior of Tfn pharmacokinetics as imaged by commercial optical system using Transferrin-Vivo 750 (PerkinElmer, USA) [20].

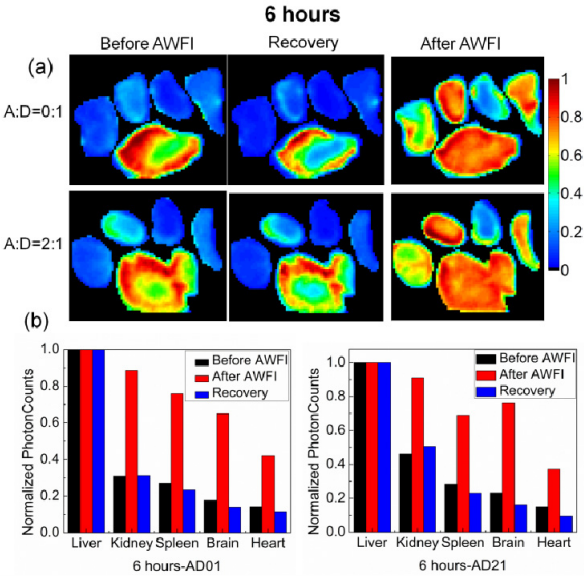

Fig. 6. Comparison of normalized fluorescence intensities of five organs (Liver, kidney, spleen, brain and heart) at post 6-hour injection. (a) Normalized fluorescence intensity images of the five organs at A:D = 0:1 and A:D = 2:1, including the fluorescence images before AWFI, the recovery image, and fluorescence image after AWFI. (b) Comparison of normalized photon counts from five organs at A:D = 0:1 and A:D = 2:1. A:D = acceptor to donor ratio.

#197596 - $15.00 USD Received 14 Nov 2013; revised 20 Jan 2014; accepted 31 Jan 2014; published 27 Feb 2014

Note that the organs with low signal always have a higher brightness before than that after AWFI. For example, the photon counts of the heart at 24 hr-AD21 in Fig. 7(b) after AWFI was reduced by 50%. This is attributed to the noise characteristics of the imaging platform. As for every photon counting technique, the noise level is non-linearly related to the detected photon counts with a decrease in SNR at low photon counts. In the case of low signals such as the one encountered before AWFI, the mean photon count values include additive signals such as noise and bleedthrough from the laser. These additive signals have minimal impact at high photon counts. Hence, after normalization, the normalized photon counts for organs with low concentration of the molecular probe exhibit lower normalized photon counts. This exemplifies the ability of AWFI allows to quantitatively retrieve low level concentration (as expected due to SNR) with higher accuracy.

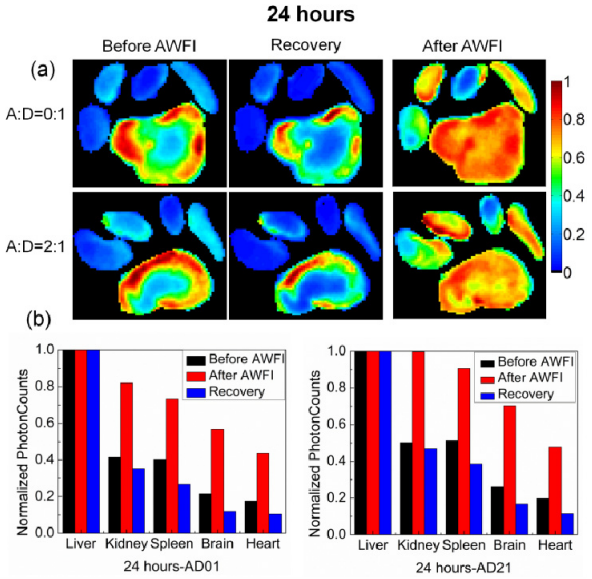

Fig. 7. Comparison of normalized fluorescence intensities of five organs (Liver, kidney, spleen, brain and heart) at post 24-hour injection. (a) Normalized fluorescence intensity images of the five organs at A:D = 0:1 and A:D = 2:1, including the fluorescence images before AWFI and the recovered image, and fluorescence image after AWFI. (b) Comparison of normalized photon counts from five organs at A:D = 0:1 and A:D = 2:1. A:D = acceptor to donor ratio.

3.3 FRET analysis of ex vivo biodistribution

FRET affects the fluorescence intensity and lifetime of the donor. If FRET occurs, the fluorescence intensity of the donor is reduced, while the lifetime of the donor is shortened. In this work, the fluorescence signals from donor were detected using the same detector gain and integration time for all the cases, but with different laser powers. The laser power is linearly dependent on the fluorescence signals. Thus, the fluorescence intensity from all the cases can be multiplied by a scalar determined by the laser power to retrieve the relative brightness of different organs at various A:D ratios from different time points (see Fig. 8). As shown in Fig. 8, the fluorescence images before AWFI and the recovered images were corrected by a scalar determined by the laser power. The fluorescence signals from 6hr-AD21 are weaker than those from 6hr-AD01 due to the FRET quenching. The fluorescence signals from 24hours are weaker than those from 6 hours due to the organ clearance. However, the fluorescence intensity cannot be used for distinguishing between receptor-mediated intracellular Tfn from extracellular soluble Tfn accumulating in the organs or in the blood, due to the enhanced permeability and retention (EPR) effect. Thus, fluorescence intensity cannot be used for

#197596 - $15.00 USD Received 14 Nov 2013; revised 20 Jan 2014; accepted 31 Jan 2014; published 27 Feb 2014

quantitative determination of intracellular amounts of internalized receptor-bound Tfn uptake for different organs.

In our previous work [16], we have demonstrated that this designed FRET NIR pair is able to discriminate the bound and internalized Tfn from free, soluble Tfn. We also have shown that the FD% indicates the fraction of intracellular receptor-bound Tfn, which includes receptor bound-Tfn at the plasma membrane as well as during clathrin-mediated internalization and subsequent endocytic recycling pathway back to the plasma membrane. Since Tfn bound to its receptor can continue to FRET during the endocytic recycling of the Tfn-TfnR complexes, FD% is able to measure the level of intracellular uptake of Tfn in different organs.

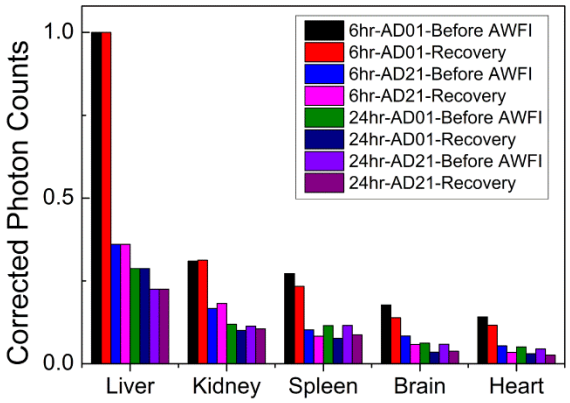

Fig. 8. Fluorescence intensity based analysis of *ex vivo* distribution. The photon counts were calculated for five organs (Liver, kidney, spleen, brain and heart) from the fluorescence images before AWFI and recovered images, and then the photon counts were corrected based on the laser powers used for each case: 6hr-AD01, 6hr-AD21, 24hr-AD01, 24hr-AD21.

As shown in Table 1, the FD% of liver, kidney, spleen, brain and heart at 6 hours with following characteristics: 1) The spleen has the largest FD% at A:D = 2:1. 2) FD% at A:D = 2:1 from the brain and liver are second only to the spleen. 3) The FD% at A:D = 2:1 from the kidney is relatively less. 4) The heart has smallest FD% at A:D = 2:1, and it is close to the FD% at A:D = 0:1. For post 24-hour injection (see Table 2), the FD% of liver, kidney, spleen, brain and heart with following characteristics: 1) The liver has the largest FD% at A:D = 2:1. 2) FD% at A:D = 2:1 from the spleen is second only to the liver, followed by brain. 3) FD% at A: D = 2:1 from the kidney and heart are very weak, and they are close to the FD% at A:D = 0:1.

TfnR is predominantly expressed in liver and it is also expressed in kidney, spleen, brain and very low expression in heart [13, 21–24]. Thus, the heart is expected to exhibit much less internalization of Tfn than the other four organs. This is consistent with our results. Our biodistribution results of FRET NIR pair match previous results [13, 21–24] suggesting that upon injection of radioactively or fluorophore labeled Tfn into nude mice, and the labeled Tfn can pass freely through various tissues and reach epithelial- and phagocytic-rich organs, such as liver, and spleen and kidney, rapidly. During circulation, the Tfn is potentially taken up by phagocytic cell-rich organs, such as liver and spleen leading to their clearance after phagocytosis from the animal [13, 21–24]. Although FD% signal at 6hr- post injection is detected mainly in liver, spleen and brain tissues with high Tfn uptake, the FD % signal after 24hr- post injection remains predominantly in the liver indicating the importance of this organ in the metabolism and catabolism of Tfn.

#197596 - $15.00 USD Received 14 Nov 2013; revised 20 Jan 2014; accepted 31 Jan 2014; published 27 Feb 2014

3.4 Active illumination for in vivo biodistribution

Next, we applied the AWFI for imaging *in vivo* biodistribution. A live mouse injected with A:D = 2:1 for 6 hours was anesthetized and placed in the supine position for imaging. The bladder and liver were imaged in the same FOV (40mm × 30mm). The AWFI algorithm stopped when the laser power was up to maximum value, without achieving the pre-defined photon count. To ensure that the performance evaluation before and after AWFI is consistent, another mask indicating the two organs was generated from the fluorescence image (see Fig. 9(b)). As shown in Fig. 9 (a) and Media 3 (FOV is shown in red rectangle), the mean photon counts of the two organs reach a plateau with increasing iteration numbers. The AWFI converges after 6 iterations. The total acquisition time was 100.8s (① Fluorescence acquisition for optimization, 1 time gate × 800 ms × 6 iterations = 4.8 s. ② Optimal fluorescence measurement, 120 time gates × 800 ms = 96s).

As expected, the bladder and liver have various fluorescence intensities due to the different locations and uptake. Figure 9(b) shows that the liver cannot be resolved by the detector before AWFI. After AWFI, both liver and bladder can be observed. The fluorescence measurement obtained using the initial pattern had a dynamic range of 33% (a ratio between the largest and smallest photon counts captured from the two organs). After AWFI, the dynamic range was reduced to less than 4%. To retrieve the true relative brightness of the two organs, the recovered fluorescence image was generated by normalizing the fluorescence image after AWFI to the excitation image of the mouse obtained from the corresponding illumination pattern. As seen in Fig. 9(c), the recovered fluorescence intensities are consistent with the normalized ones before AWFI. FD% is also evaluated by Eq. (1) (see Fig. 9(d)) and the FD% after AWFI for liver (FD % = 26 ± 4) is consistent with the one from the *ex vivo* liver.

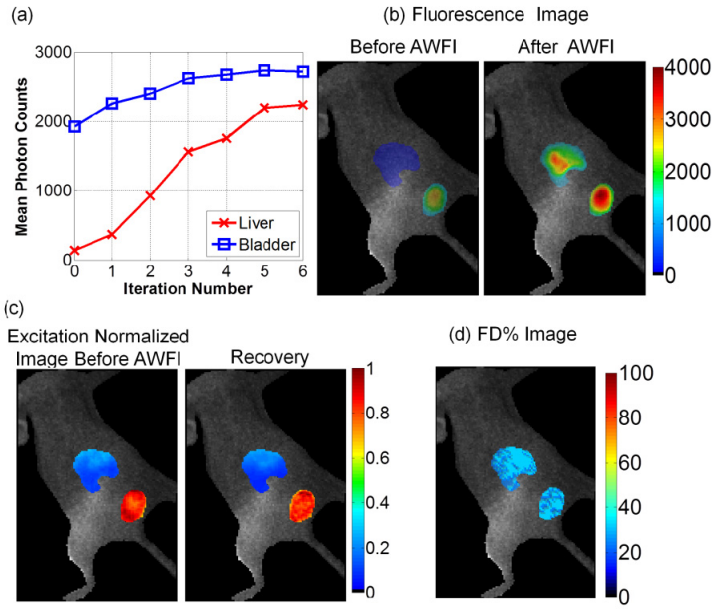

Fig. 9. AWFI for *in vivo* imaging using a live mouse injected with 6-hour post injection at A:D = 2:1. (a) The comparison of the mean photon counts of bladder and liver versus different iteration numbers (Media 3). (b) The comparison of the excitation normalized image before AWFI and the recovered image. The excitation normalized image before AWFI: the fluorescence image before AWFI was normalized to the excitation image of the mouse obtained from the corresponding illumination pattern. (d) The distribution of FRET donor fraction (FD %) at A:D = 2:1.

#197596 - $15.00 USD Received 14 Nov 2013; revised 20 Jan 2014; accepted 31 Jan 2014; published 27 Feb 2014

Herein, we have for the first time applied AWFI for *in vivo* imaging to acquire optimal fluorescent data set to improve SNR, weak-signal sensitivity and dynamic range caused by the spatial distribution of organs, animal thickness and optical parameter characteristics. More importantly, the preliminary results presented here establish the feasibility and the applicability of this technique for whole-body live animal imaging. The fact that we can image Tfn uptake by normal epithelial organs such as liver and bladder in a live animal has crucial significance in a wide range of applications including but not limited to cell signaling, protein biology and evaluation of various therapeutics.

The application of AWFI technique described in this paper is directed toward planar time-resolved fluorescence imaging. However, it is worth noting that this approach can be readily translated to *in vivo* fluorescence molecular tomography (FMT). In our previous work [14], we have implemented AWFI to the excitation field of a synthetic animal model for FMT to increase SNR and the tomographic information. The AWFI described in this paper has additional advantages. First, this DMD-based spatial light modulator provides higher resolution (1024 × 768), higher transmitted power efficiency (increased by 3.5 times) and more linear relationship (within 3% of fidelity) with expected grayscale. Second, this AWFI improves fluorescence signals by directly being applied to fluorescence field. Third, this AWFI reduces overall acquisition time by optimizing the illumination pattern based on only one fluorescence image at each iteration except the last one. Last, this AWFI is more sensitive to multiple targets in one FOV by calculating the laser power modification factor based on each individual target, instead of the whole FOV, which has been successfully applied for multi-well plate imaging [11]. Thus, the improved AWFI described in this paper makes it more feasible for *in vivo* FMT. Ongoing studies in the laboratory will apply this AWFI to *in vivo* FRET tomography to improve the estimation of FRET efficiency in whole body live mouse imaging. Although much research remains to be conducted, it appears that this technique has a great potential to provide the accurate estimates of FD% due to the higher SNR of the measurements, but also improve the signal level at the time gates on the early-rising and falling portion of the TPSF (see Fig. 10 and Media 4) for high-resolution optical reconstruction and discriminating FRET donor from non-FRET donor with lower crosstalk, respectively.

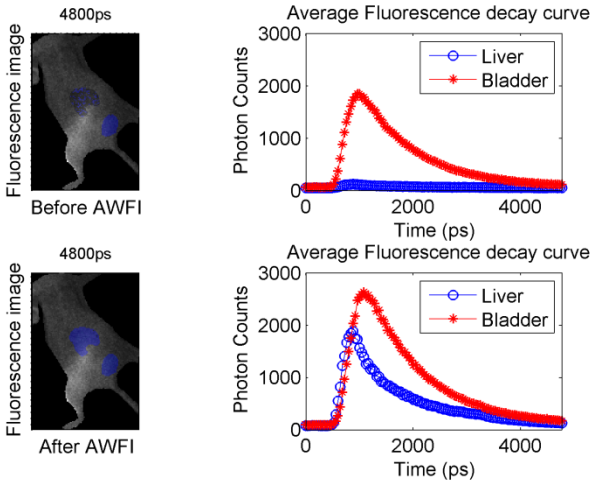

Fig. 10. Excerpt from video showing the fluorescence images before AWFI and after AWFI at the corresponding delay time from the TPSF of the liver and bladder (Media 4).

#197596 - $15.00 USD Received 14 Nov 2013; revised 20 Jan 2014; accepted 31 Jan 2014; published 27 Feb 2014

4. Conclusion

AWFI can capture optimal fluorescence measurements over a large area by optimizing the illumination pattern and overall laser power on the region of interest. AWFI enhances the dynamic range of the imaging platform and hence the SNR of acquired data. Since AWFI is able to obtain an optimized fluorescence intensity distribution, it can be applied to both lifetime imaging and fluorescence intensity measurement. Herein, we demonstrated the ability of AWFI to accurately estimate FRET signals from different dissected organs. We further reported its successful application to quantitative FRET in live mice imaging. We demonstrate that AWFI can improve the accuracy of fluorescence decay curve fitting in *ex vivo* biodistribution of different organs and *in vivo* biodistribution in live mice. Overall, this method allows for enhanced accuracy in lifetime-based studies, at a high acquisition speed, and over samples with a wide range of fluorescence intensities. This is very significant for quantitative fluorescence lifetime imaging applications, such as lifetime comparison of different solvent viscosities [25] or lifetime comparison of different pH values [26] or FRET efficiency comparison of different A:D ratios [9]. We expect that AWFI can be applied to the non-scanning fluorescence imaging system in the reflectance mode and continuous-wave (CW) mode and other biomedical applications such as image-guided surgery. Furthermore, AWFI can be implemented in multi-view settings for tomography and/or with structured patterns for direct quantitative measurements [9, 27].

Acknowledgments

This work was partly funded by the National Institutes of Health grant R21 CA161782-01 and National Science Foundation CAREER AWARD CBET-1149407. We would like to thank Dr. Robert Waniewski and Dr. Timothy Quinn at the Bioresearch Core for their helpful comments and assistance with the animal work.

#197596 - $15.00 USD Received 14 Nov 2013; revised 20 Jan 2014; accepted 31 Jan 2014; published 27 Feb 2014